SAND2020-1988J

IMAGING PERTURBED SHOCK PROPAGATION IN POWDERS

M.A. Cooper*,#, A.W. Sapp*, S. Guo*, T.J. Vogler†

* Explosive Technologies, Sandia National Laboratories, Albuquerque, NM, USA 87185

† Mechanics of Materials, Sandia National Laboratories, Livermore, CA, USA 87185

Corresponding author: macoope@sandia.gov

A novel experimental methodology is presented to study the deviatoric response of powders in shock regimes. The powders are confined to a cylindrical wedge volume and a projectile-driven shock wave with a sinusoidally varying front propagates through the powder. The perturbed shock wave exhibits a damping behavior due to irreversible processes of viscosity and strength (deviatoric) of the powder with propagation through increasing powder thicknesses. The inclined surface of the wedge is polished and coated to establish a diffuse surface suitable for reflecting incident laser light into a high-speed camera imaging at 5 MHz. Images of the contrast loss upon shock wave arrival at the observation surface are post-processed for qualitative and quantitative information. New data of shock damping behavior with parameters of perturbation wavelength and initial shock strength are presented for powders of copper, tantalum, and tungsten carbide as well as their mixtures. We present the first full-field images showing additional spatial disturbances on the perturbed shock front that appear dependent on particle material and morphology.

Keywords: shock perturbation, planar impact, gas gun, high-speed imaging, edge tracking, powder compaction

INTRODUCTION

A new experimental method has been developed to study the deviatoric response of powders in shock regimes. Shock waves in planar geometries have been used extensively to understand dynamic powder compaction [1, 2]. These planar tests measure the dynamic longitudinal stress-density response but information about the material strength (deviatoric) response is not known. If the propagating shock wave is non-planar, such as a sinusoidally-perturbed shock wave, it is damped by irreversible processes of viscous flow and plastic deformation within the medium. The damping behavior of a perturbed shock wave has been used extensively in literature to measure the viscosity of arbitrary fluids. Some of this earliest work was performed in air [3] and metals [4]. A review of the literature for liquids and solids appears in Vogler [5] along with our first efforts studying the damping behavior of perturbed shock waves in powders.

In optically accessible fluids such as air, imaging the spatially varying front of the perturbed shock wave is straight forward. Observation of the shock front is aided by schlieren imaging through the fluid along the direction perpendicular to shock propagation [3]. In solids, optical and electrical methods detect the shock front motion at

material boundaries. Mineev and Savinov photographically recorded spatially continuous records of the perturbed shock with a fluorometric device [4]. Ma et al. record the arrival time of the perturbed shock at an array of electric pins with discrete spatial positions [6]. Observing the perturbed shock damping behavior in powders requires a new approach as the powder and containment fixturing is optically opaque and the perturbed shock pressures studied are relatively low compared to literature in solids.

A light gas gun facility is used to launch a projectile into a cylindrical wedge target containing powders at their tap density. The base of the cylindrical wedge target is machined with a wavy pattern generating a perturbed shock wave that propagates through the granular material. The perturbed shock wave transmitted through the granular material creates a visible wavy pattern on the inclined boundary of the wedge target that is imaged at high speed and post-processed for quantitative data extraction. Prior work observing explosively-driven shock wave arrival at sample boundaries has relied on shock-luminescent indicators from a trapped gas or a light enhancing coating [4, 7]. For our projectile-driven shock waves, the shock pressures in the granular material are insufficient to activate adequate light emission by these methods. Instead, our early work applied Optically Recording Velocimetry Interferometer System (ORVIS) [8] to observe perturbed shock damping behavior in planar samples [5, 9]. We observed that arrival of the perturbed shock wave at the observation surface caused a complete loss of reflected laser light at the camera. Because a thin layer of buffer material was used to protect the reflective observation surface, the wavy pattern is responsible for imparting a directionality to the reflected laser light precluding collection into an interferometer [9]. Others have also used this laser diagnostic in tests with metals with similar observations of prompt reflectance loss at the imaging surface [10]. The complete loss of light was convenient for post-processing edge detection of the perturbed shock front but coupling to the interferometer was an unnecessary complexity. In the present study, we capitalize on the known loss of reflectivity at the window associated with shock wave arrival and apply a non-interferometric imaging method.

Simple high-speed imaging using modern charge-coupled device (CCD) camera technology was applied to the shock conditions within the powder beds studied here. This work is the first demonstration of capturing full field, two-dimensional image data from samples with varying thickness in a single shock experiment at sub-microsecond rates. This experimental methodology has been under development for several years and is now a routine testing and analysis capability at Sandia National Laboratories. Our work was largely focused on tungsten carbide (WC) as an extension to prior research where the dynamic longitudinal stress-density response of solid carbides was measured and modeled [11, 1, 12]. Tungsten carbide was also initially used in the early perturbed shock experiments with powders [5]. Here, new data on powders of copper, tantalum, and tungsten carbide as well as their mixtures are presented.

MATERIALS

The experimental powders varied in terms of material, volume fraction, morphology, and size. Scanning electron microscope (SEM) images of the four tested powders appear in Figure 1. Powders of tungsten carbide (WC), tantalum (Ta), copper (Cu), and a 50/50 wt% WC/Ta mixture were studied to explore critical parameters dominating perturbed shock behavior. Other than Cu, the as-received powders were sieved to remove particle sizes greater than 32 μm and less than 20 μm. Because of the different particle morphologies, the ASTM E11 sieves passed some particles with sizes greater than 32 μm and less than 20 μm as quantified with a Beckman Coulter LS 13 320 laser diffraction particle size analyzer. The solid densities of the materials and measured particle size distributions appear in Table 1. For the data of Table 1, multiple tests were performed with the WC material and a single test was performed with the Cu, Ta, and WC/Ta materials (See Appendix A and Appendix B).

The WC was obtained from Kennametal Inc. of Latrobe, Pennsylvania (Figure 1a) [1, 5]. The Ta was obtained from American Elements, Part number TA-M-025M-P.325M (Figure 1b). A WC/Ta mixture was created by mixing equal weights of the two dry WC and Ta powders in a rotating jar. The copper was obtained from Materion (Figure 1d).

Table 1. Solid density ρ_s, bulk sample density ρ_{00}, and solid volume fraction ϕ. Measured particle size distribution (μm) by mass of experimental powders.

	ρ_s (g/cm^3)	ρ_{00} (g/cm^3)	$\phi = \rho_{00}/\rho_s$	Particle Size Distribution (μm)				
				<10%	<25%	<50%	<75%	<90%
WC	15.6	8.73	0.53	23.3	27.6	33.0	39.3	46.2
Ta	16.7	5.45	0.33	7.9	18.7	27.0	35.1	43.0
WC/Ta	16.1	6.97	0.43	24.6	30.0	36.4	43.9	52.1
Cu	8.96	5.50	0.61	60.1	66.1	72.7	79.8	88.0

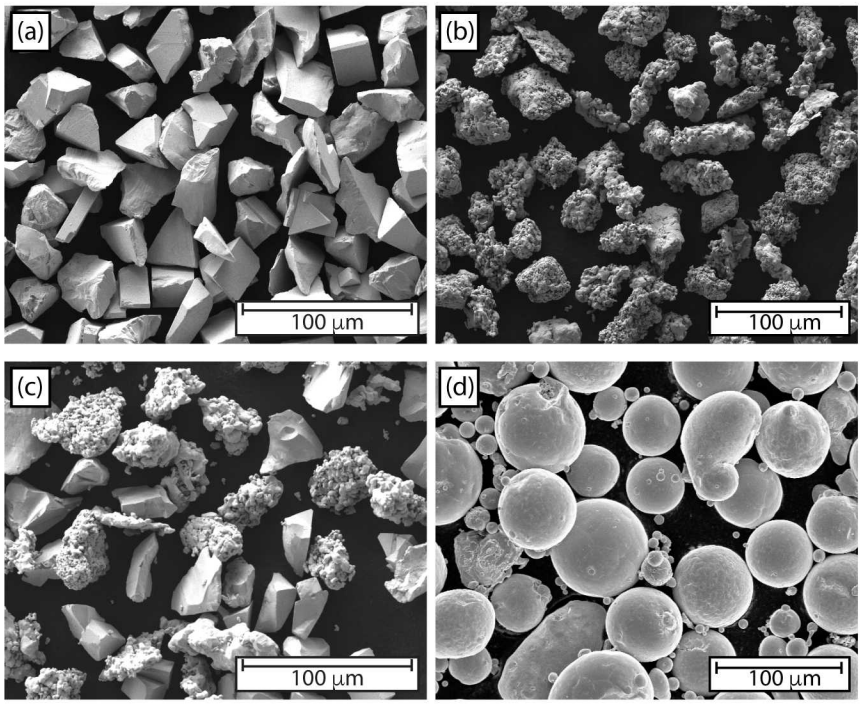

Figure 1. SEM images of experimental powders. (a) tungsten carbide, WC, (b) tantalum, Ta, (c) 50/50 wt% tungsten carbide and tantalum, (d) copper, Cu.

EXPERIMENTAL SETUP

The experimental powders were confined within a cylindrical wedge and a shock wave was driven into the powder sample by projectile impact in a light gas gun facility (Figure 2). The light gas gun facility consists of a single-stage gas gun with an 18-meter-long barrel, which drove an aluminum projectile (63.5-mm diameter) at a velocity of either 0.5 km/s or 0.9 km/s into the target assembly. The base of the gas gun target is an aluminum driver plate machined with a sinusoidal wavy pattern (annotated as Wavy Driver in Figure 2). Upon symmetric impact of the flat face of the projectile with the flat face of the driver plate, a shock wave is generated and passes through the wavy driver plate and into the powder sample. The shock wave, perturbed by the sinusoidal shape of the driver-powder interface, passes through the powder sample in the direction of increasing thickness. The transmitted shock wave interacts with an observation surface formed by plating the mating surface of a poly(methyl methacrylate) (PMMA) window. Laser illumination through the window results in reflected laser light that is directed into a high-speed camera imaging the entire observation surface. The arriving shock wave disrupts the reflectivity of the observation surface, providing a visual, spatially-resolved indicator of shock wave arrival. The next sections describe details of the gas gun target, pre-test alignment, test execution, and high-speed imaging.

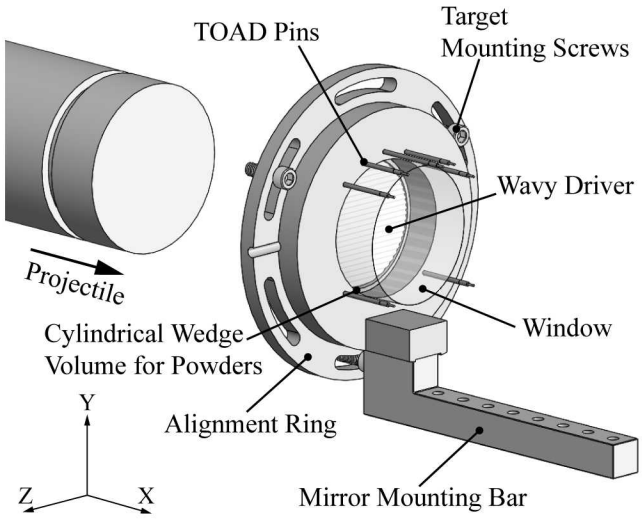

Figure 2. Illustration of experimental gas gun target for confining powders in a cylindrical wedge volume. A shock wave is generated in the gas gun target by impact of a 63.5-mm-diameter projectile.

Target Design

The gas gun target is assembled from an alignment ring, driver plate, window, powder sample, TOAD (Time of Arrival Device) pins, and mirror mounting bar (Figure 2). The alignment ring (Figure 3) contains a through hole with diameter of 47.625 mm. A blind counterbore hole is cut into the impact side of the target to receive the driver plate establishing a solid, flat surface for projectile impact. The opposite side of the alignment ring is machined with a second blind counterbore hole, creating a recess to seat the 50.8-mm-diameter, 25.4-mm-thick window. This 'window bore' is tilted at $\theta = 4.5°$ from the axis of the initial through hole (which is perpendicular to the impact surface). The window is tilted about the Y axis such that the thin "toe" of the cylindrical wedge volume crosses the negative Z axis and the thickest "heel" of the cylindrical wedge volume crosses the positive Z axis (Figure 2). The driver plate and window are glued to the alignment ring using Loctite Hysol thin film epoxy (Hardener, HD3475; Resin RE2038).

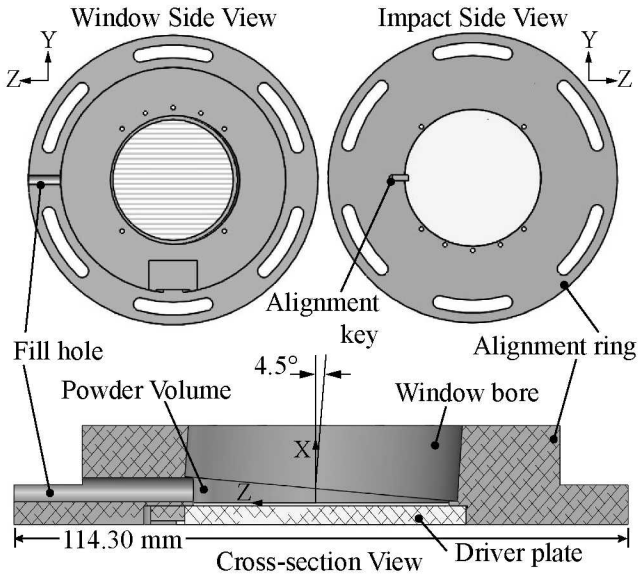

Figure 3. Side and cross-section views of the assembled alignment ring and driver plate components of the experimental gas gun target.

The aluminum driver plate is wire electrical discharge machined (EDM) with a sinusoidal wavy pattern forming a series of peaks and troughs (Figure 4). The amplitude of the pattern, $2a_0$, was nominally 0.5 mm. The wavelength of the pattern, λ, was nominally 1, 2, or 4 mm. Measurements of the as-machined pattern were collected with a Form TalySurf® PGI 2000S surface measurement system (Table 2). Our initial driver plates contained patterns at a single wavelength (driver type B-D in Table 2). Later, the driver plate (driver type E in Table 2) was split into three regions each with a sinusoidal pattern of different wavelengths. An equal number of wavelengths was in each region. One driver plate (driver type F in Table 2) was fabricated without a wavy pattern; representing a flat driver typical of gas gun testing.

The nominal dimensions of the wavy driver SolidWorks® model were updated with the as-machined driver plate measurements to calculate the volume filled with powder (Table 2). Figure 5 illustrates this cylindrical wedge volume formed from surfaces of the alignment ring, the inclined window surface, the patterned surface of the wavy driver and the fill tube. The powder volume is nominally 0.81 ± 0.03 mm thick at the wedge toe and 4.57 ± 0.03 mm at the wedge heel as measured from the troughs of the wavy pattern. The fill hole is cut into the alignment ring for access to the heel of the cylindrical wedge powder volume. The powder is loaded into a syringe and poured through the fill hole while vibrating with a dental vibrator until the powder sample is at a stable density (Table 1). The total powder mass is measured, and the fill hole is sealed with a small amount of Devcon 5 Minute® epoxy. Thus, the powder is sealed within the target assembly along with air at ambient pressure (nominally 86 kPa in Albuquerque, New Mexico, USA).

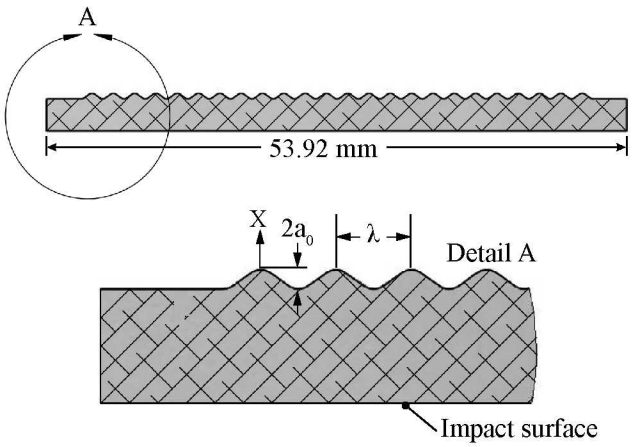

Figure 4. Side view of the entire wavy driver plate (top) and an enlarged view of the sinusoidal pattern with known amplitude and wavelength (bottom).

Table 2. As-machined driver plate details of sinusoidal amplitude ($2a_0$) and wavelength (λ). Volume is calculated from the solid model using the as-machined driver plate measurements.

Label	$2a_0$ (mm)	λ (mm)	Volume (cm^3)
Fill Tube	-	-	0.24
B1-B5	0.42	1.98	4.51
B6-B15	0.49	1.98	4.59
C1-C3	0.52	3.96	4.59
D1-D3	0.49	0.99	4.59
E1-E3	0.53	0.99, 1.98, 3.99	4.59
F1	0.00	none	5.04

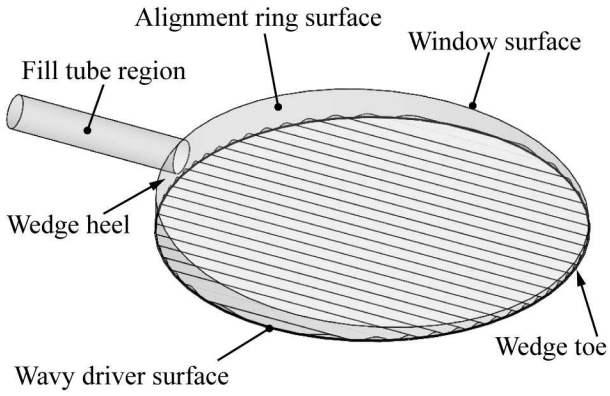

Figure 5. Illustration of powder region between confining surfaces of wavy driver, window, alignment ring and fill tube. This calculated volume is used to calculate bulk powder density.

To ensure proper rotational alignment of the wavy pattern with the inclined window surface, a rectangular slot is cut into the impact surface of the alignment ring and driver plate enabling installation of an alignment key (see Impact Side View of Figure 3). Tolerancing of the slot and alignment key results in alignment of the wavy pattern

to the Z axis (Figure 2) within 4.3 milliradians. A Starrett 135A precision level is used to confirm the rotational alignment of the target assembly with the Z axis (Figure 2). Typical machining tolerances of perpendicularity, parallelism, and flatness for the impact surfaces of the alignment ring, driver plate, and projectile along with traditional gas gun alignment methods yield impact planarity within 1-2 milliradians.

Window Surface Preparation

The primary diagnostic is high speed imaging of the observation surface created by plating the PMMA window. The optimum surface for high speed imaging of the reflectivity loss was a mild treatment to the PMMA window resulting in the appearance of a slight haze at the surface. To achieve this result, the impact side of the window is treated using an Airbrasive 6500 sand blaster loaded with Accubrade 27, Blend #1 alumina blasting media. The process involves spacing the blasting pen nozzle nominally 80 mm away from the window surface, which is slowly rotated as the spray is passed back and forth across the surface for 10 passes. The window is rotated, and the process is repeated 8 times. Once this is complete, the window is cleaned, and an aluminum film is plated onto the treated surface. A plating thickness of h = 0.4 μm (a typical thin coating) or h = 22 μm (thickest coating possible with Sandia's plating capabilities) was used for exploring the effect of plating thickness on captured image features. This combination of blasting and aluminum coating yields a uniformly diffuse surface on the inside of the window that is devoid of specular reflections and directional patterns that can corrupt computational edge detection in the experimental images (Figure 6).

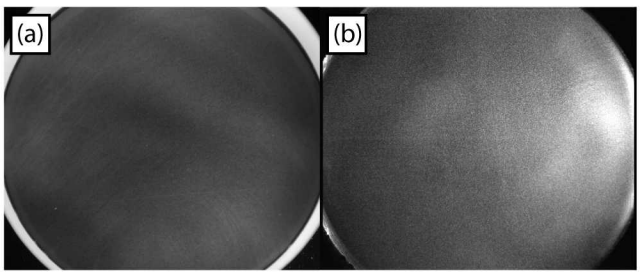

Figure 6. Representative window surface showing (a) broadband and (b) laser light inspection images.

Optical Imaging

The cylindrical wedge target is positioned within the target chamber of the light gas gun facility as shown in Figure 7. The wedge target is mounted at the end of the barrel (not shown) and is impacted as previously discussed by the projectile. The impact surface of the driver plate is parallel with the Z axis and the direction of shock propagation through the cylindrical wedge powder sample is in the X-axis direction. The sample wedge toe crosses the negative Z axis and the wedge heel crosses the positive Z axis. A side chamber window is used to pass the incident light from the SI-LUX640 laser illuminator into the chamber which is then reflected onto the inclined observation surface by a turning mirror mounted on the target mirror mounting bar. The reflected laser

light is directed to the camera by the same internal turning mirror and a second turning mirror outside of the chamber.

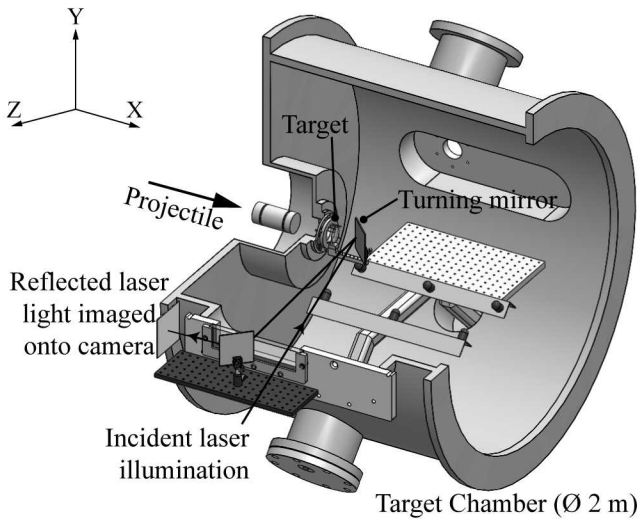

Figure 7. Experimental arrangement at target chamber for high speed imaging.

The SI-LUX640 laser illuminator is a 400 W, 640-nm continuous wave laser that is pulsed using an auxiliary output (Aux Out) signal from the Kirana (Specialised Imaging) high speed camera operating at 5 MHz. The Kirana exposure was set to 200 ns (1/frame rate of 5 MHz). The Aux Out signal was set in the camera control software to a minimum 10 ns delay from the start of the exposure and a pulse width between 25-40 ns seconds which varied based on the individual window reflectivity of each target.

Illumination of the tilted, 50.8-mm-diameter window utilized an intentionally misaligned laser beam to obtain nearly-uniform illumination across the target and to accommodate the geometric constraints of the target chamber boundaries along the illumination and imaging paths. An achromat lens (f.l. 300 mm) was located immediately outside the target chamber window and reduced beam expansion over the nearly 1-meter path length to the target. Figure 8a-b show static images of two pre-test targets with nearly full, uniform illumination obtained by aligning the main laser spot off either the heel or the toe of the target. With the main laser spot aligned to the target, a lens arrangement outside the target chamber was not possible to expand the beam to illuminate the entire target window. Adjustments to the lens aperture with the shortest 10-ns laser pulse duration resulted in a center region of the target window to be saturated or nearly saturated. This is illustrated in comparing the "on-target" beam profiles extracted from a row of image pixels intensities plotted in Figure 8c. By moving the beam spot "off-target", increasing the laser pulse duration, and opening the lens aperture (f/4), the entire target window was illuminated with nearly constant pixel intensities.

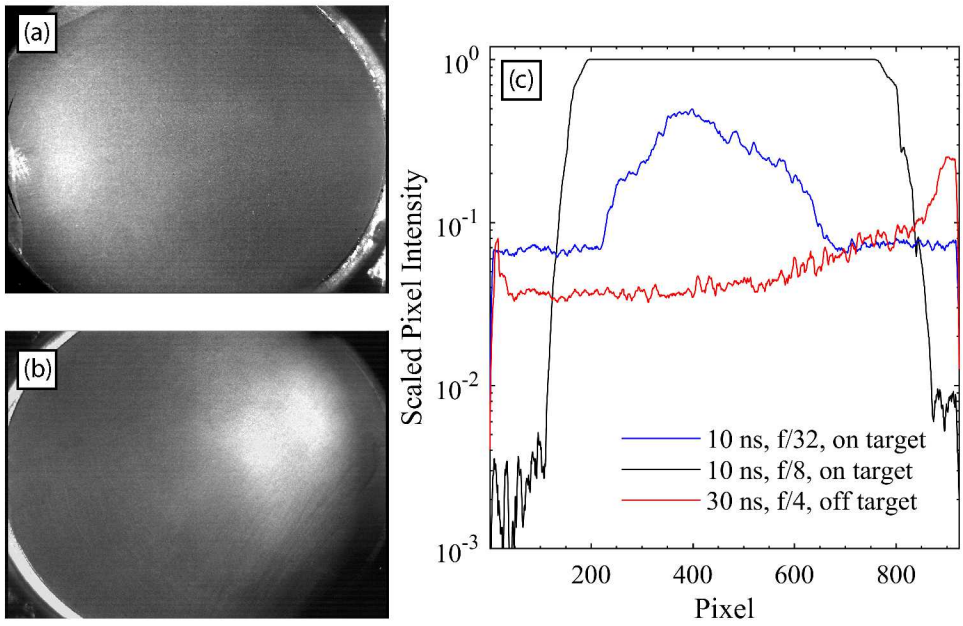

Figure 8. Static images of the pre-test target showing the illumination gradient with bright spot off the (a) heel or (b) toe of the cylindrical wedge target. (c) Scaled pixel intensities for different illumination schemes showing the full and nearly uniform illumination obtained with an intentional mis-alignment the main laser beam.

The field of view and magnification were determined during pre-test alignment using a specially prepared calibration window. The calibration PMMA window contained a precise grid of laser-machined dots at the plated surface. The dots appear dark in the camera images, and their spatial frequency in the vertical and horizontal directions was determined by 2-D fast Fourier transform. The Kirana camera captured images with 924 × 768 pixel resolution and the image magnification was between 18.5-20.5 pixels/mm depending on the total imaged field of view for each test. An optical resolution of the imaging system equal to 4.00 lp/mm was measured with the 1951 USAF resolution test chart.

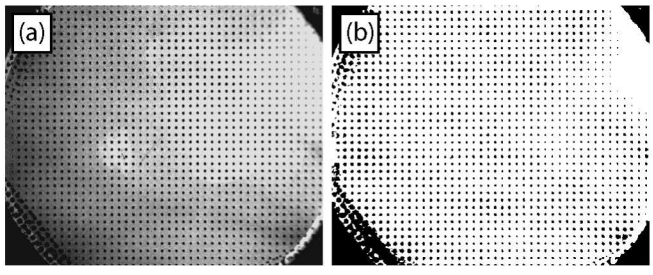

Figure 9. Calibration window with laser-machined dots for image magnification calculation. (a) Kirana image of alignment window and laser illumination. (b) Binary image with detected grid points for frequency analysis.

Experimental triggering began with the projectile, traveling at either 0.5 or 0.9 km/s, impacting the protruding timing pins. One of the timing pins protruded from the target alignment ring a distance based on the intended impact velocity to generate a trigger signal nominally 11 microseconds before projectile impact. This trigger

signal started Kirana camera capture of the 180-frame image sequence. With other associated cable delays and time through the target, the images of shock motion appeared during frames 65-80 of the 180-frame image sequences.

PERTURBED SHOCK FEATURES

The sequence of images collected by the Kirana camera at high speed captured the passage of the perturbed shock wave across the target window. Shock arrival caused a reflectivity change at the plated window surface which appeared as a contrast discontinuity in the camera image. The thin plated coatings were found to be easily removed by gentle wiping with a tissue. Thus, it is expected that the neighboring particles at shock pressures would mechanically remove the plated coating. Another mechanism could be associated with a change in surface roughness attributed to the deformable PMMA window [9]. The sharpness of this contrast change is closely coupled to the laser pulse duration. With optimum alignment and reflecting window surface, laser pulses as short as 25 ns produced suitable pixel intensities for image analysis.

The Kirana camera has known issues of ghost images from the prior frame and 10-frames prior; as well as a pulsation of the mean image intensity that occurs over a 10-frame cycle. The ghost images consisted of the sinusoid pattern from prior frames (-1, -10) superimposed on the post-shock, dark region of the current image. All images were post-processed to remove the ghosting and minimize the variations in mean image intensity. Because these experiments were not self-luminous and the propagating shock edge translated across the image, these corrections could be made relatively easily with no direct effect on the contrast gradient at the leading shock front.

Figure 10 presents three frames from image sequences captured from WC powders at three different values of λ. For the three image sequences shown, they have been flipped about the Y-axis to align the wave propagation from the left side of the image (toe of the wedge) to the right side of the image (heel of wedge) with increasing time. The effect of increasing λ is easily seen by comparing images between the tests. For the tests with λ equal to 2 and 4 mm, the shock front maintains a regularly varying pattern across the target and the peak/trough pixel locations remain aligned to the corresponding features of the wavy driver. For the test with λ equal to 1 mm, the pattern becomes slightly irregular after passage across about half of the target and the pattern is largely indistinguishable near the target heel.

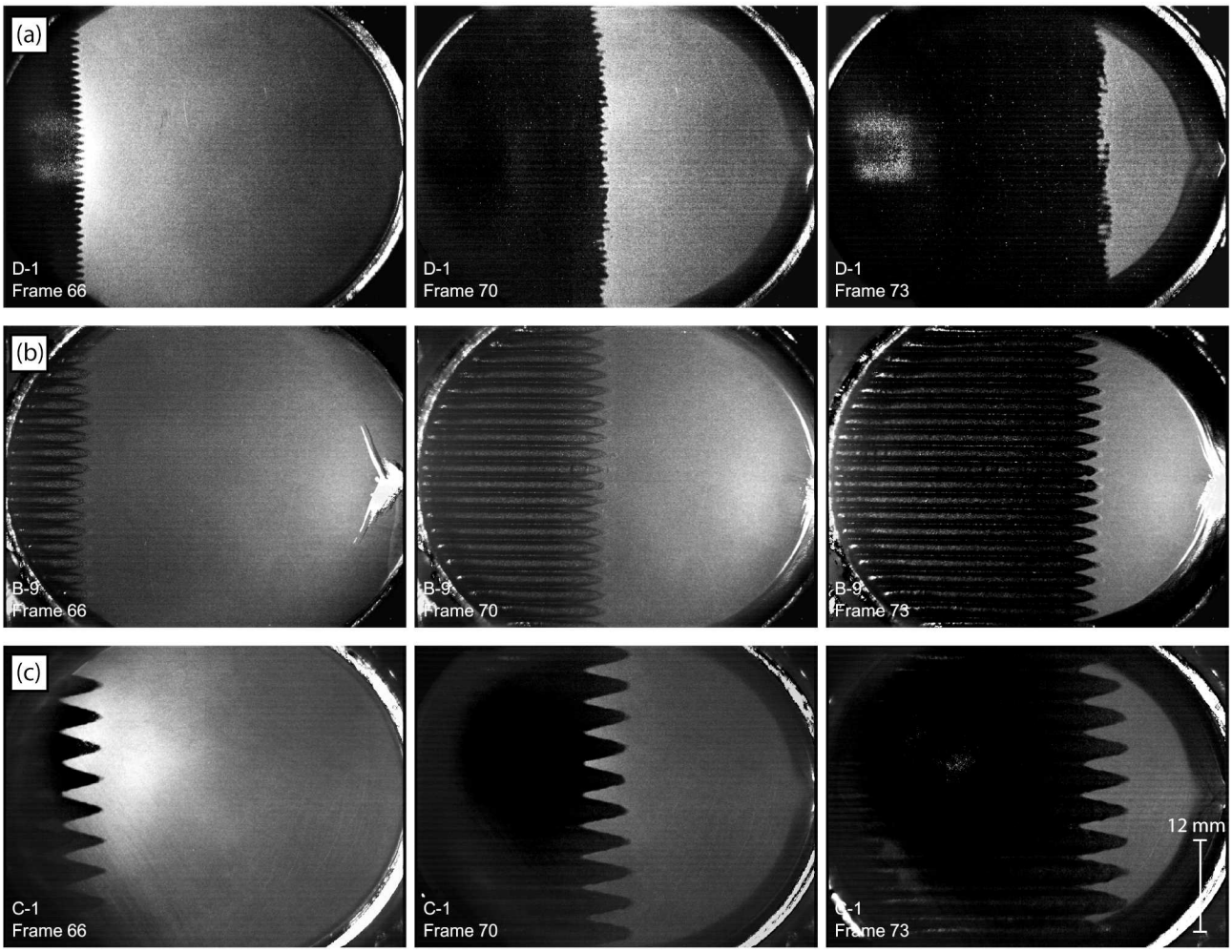

Figure 10. Frames extracted from recorded image sequences for tungsten carbide tests with different driver plate wavelength, λ. (a) D-1 with $\lambda = 1$ mm, (b) B-9 with $\lambda = 2$ mm, (c) C-1 with $\lambda = 4$ mm. Interframe time is 200 ns.

In most of the images of Figure 10, some horizontal lines are visible in the illuminated portion of the target prior to arrival of the perturbed shock wave. The wavelength between these lines is 0.8 mm at this image magnification and are not associated with any length scales of the sinusoidal perturbation. These lines are an artifact of the camera and become more obvious with severe image contrast adjustment. Under extreme contrast adjustments, they are also visible in the dark regions of the image. After passage of the perturbed shock wave for the images of Figure 10b, some reflectivity remains persistent as higher-intensity horizontal regions aligned with the peak of the sinusoidal pattern. This effect is not a camera artifact but is due to an interaction of the perturbed shock wave with the thick plated coating and the window surface resulting in some reflected laser light continued to be imaged by the camera.

A closer look at the leading edge of the shock front shows local distortions superimposed on the major perturbation imposed by wavy driver. A single frame from different tests where the wave has reached the middle

portion of the target is compared in Figure 11. These images have been cropped and compiled for ease in qualitatively comparing the shock fronts. Irregular bumps at the shock front and peak-to-tough variations appear for all the materials. It is reasonable to link these local disturbances to particle characteristics as the particles likely form a network for stress transmission through varying particulate contact networks [11]. At our imaging spatial resolution of 4 lp/mm, we are unable to resolve the shock front at the individual particle length scales. However, the effects of particle ensembles in groups of approximately 10 particles or more are resolvable. In this work, we have prioritized a field of view that captures images across a large range of sample thicknesses to study perturbation decay. Observation of these additional distributions on the main shock front was a unique discovery possible by our testing across materials and different window plating thickness. A smaller field of view and higher magnification would be useful to explore the role of individual particle morphology on the primary perturbed shock. The plastic deformation, bulk particle strength, and intergranular friction phenomena likely affect particle reorganization, fracture, and energy transport across particle contacts resulting in slight temporal variations in shock passage through the powder sample.

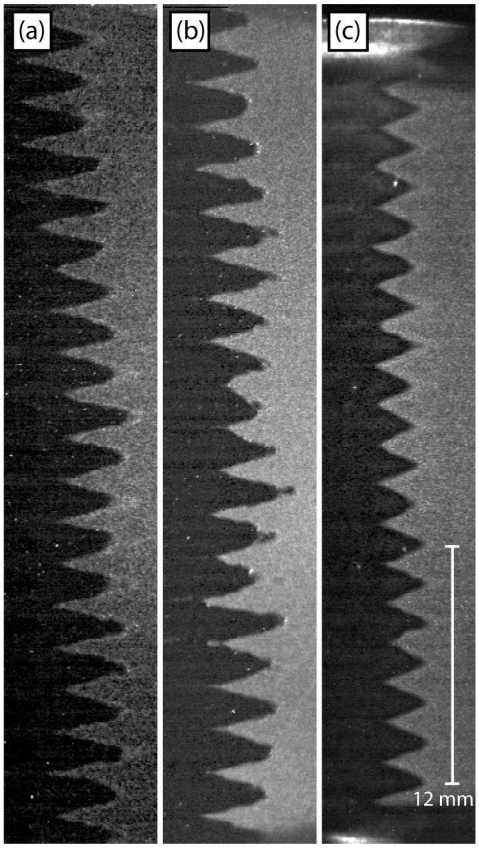

Figure 11. A closer look at the wavy pattern shapes. Local distortions were obvious on the samples. (a) WC, B-4, (b) WC/Ta, B-13, (c) Ta, B-14.

Wavy driver plates with multiple wavelengths also generated similar patterns (Figure 12). No obvious disturbances to the patterns were observed where the pattern changed from one wavelength to the next. Thus,

future testing is planning to utilize multiple wavelengths in a single driver plate to increase data return per test. To have enough cycles to analyze and account for corruption by the side relief waves, only two wavelengths on a single, 47.6-mm-diameter target are reasonable.

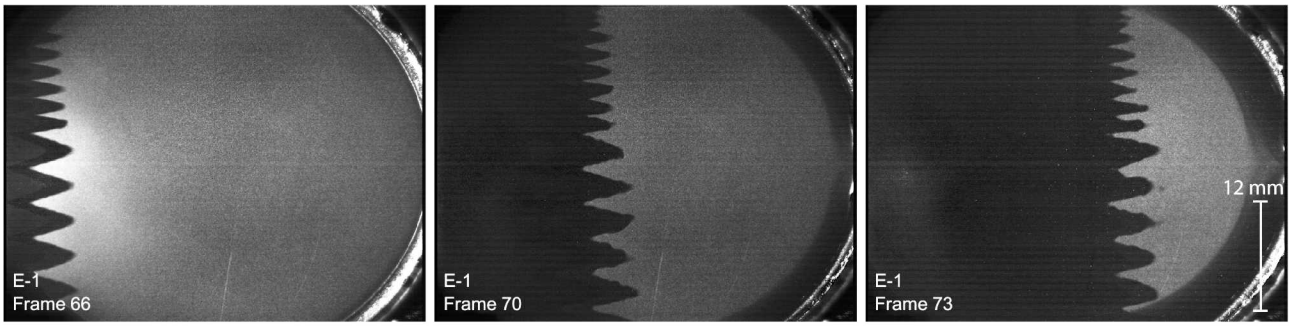

Figure 12. Frames extracted from a recorded image sequence with tungsten carbide (E-1) and a driver plate consisting of regions with different wavelength, λ (1 mm, 2 mm, and 4 mm).

Using a flat, planar driver plate (Type F of Table 2), our imaging method was applied to understand the variation of shock arrival at the observation surface due to an unperturbed shock propagating through the powder. Usually, laser velocimetry methods have been employed to study spatial and temporal variations in shock propagation through heterogeneous materials [13]. Here, a planar shock was transmitted into the powder bed, yet a spatially disturbed shock front is observed at the plated window surface (Figure 13). The disturbances on the shock front are qualitatively greater after passage through more of the powder sample. This suggests that much of the observed deviation from the initial sinusoid pattern is due to similar disturbances. Presumably these local disturbances on the primary perturbed shock would be affected by bulk density variation and particle strength. Further exploration of these powder parameters on the resulting images remains future work.

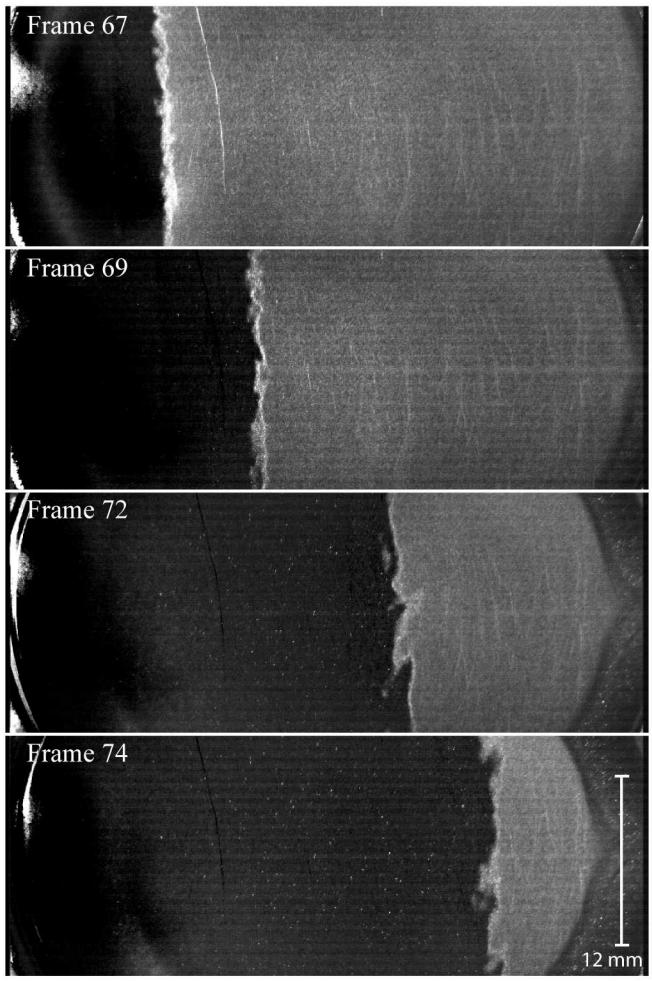

Figure 13. Image sequence of flat driver and tungsten carbide sample (F-1).

IMAGE PROCESSING TO EXTRACT SHOCK BEHAVIOR

The experimental image sequences are post-processed to detect the perturbed shape of the shock front edge along with its relative positioning on the target window. This is performed in MATLAB® with a sequence of image processing techniques for edge detection. As mentioned previously, the images within a test sequence and between sequences did not have an equal mean pixel intensity. Rather, the non-uniform illumination due to the laser alignment method, the varying reflectivity associated with the plated window surface, and a varying mean image intensity due to the camera CCD characteristics added complexity to the shock front edge detection process. Other experimental factors that were observed to affect the contrast in pixel intensities at the shock front were the impact velocity, laser pulse duration, and plating thickness. The best set of conditions for optimum edge detection were found to occur at the higher impact velocity (0.9 km/s), shortest laser pulse duration (~25-40 ns), and thinnest plating thickness (0.4 um).

Analysis of an image sequence starts by manually post-processing the raw image frames to remove the ghost artifacts attributed to the prior frame and the tenth prior frame (Figure 14a). The scaled, double precision images

were then used to detect the local change in contrast at the shock front edge. This process detects the primary shock front edge for capturing the bulk perturbation decay behavior and is not focused on capturing the local deviations discussed previously in Figure 11 for further analysis. A flat field correction was applied (Figure 14b) so that the contrast changed between a mid-range gray value intensity in the undisturbed region to a near-zero gray value in the post-shock region. Also, observed in the region of this contrast change are single pixel intensities near unity (bright pixels) that become more prominent after the flat field correction. An unconnected outline of bright pixels could be seen in the raw images of certain test sequences. It is unknown if these are associated with destruction of the plated interface during the arrival of an elastic precursor wave or due to the particle-plating-window interface behavior causing reflectivity changes focusing light onto the camera image plane. In any case, these bright pixels were treated as impulse noise and removed with a 2-D Gaussian smoothing kernel. The contrast gradient is maximized at the leading edge of the shock. A double-precision image of the gradient magnitude values using the Prewitt operator was calculated; effectively enhancing the shock front edge (Figure 14c). This gradient magnitude image was then binarized with a global threshold value obtained by using Otsu's method over a region of interest containing the shock front (Figure 14d). This binarization with a global threshold detected other "edges" from the gradient magnitude image not associated with the primary shock front edge. These were removed by series morphological transformations to remove small objects and masking areas external to the region of interest containing the shock front (Figure 14e). The result is a binary image containing only the pixels associated with the largest contrast gradient at the shock front which could be overlaid onto the beginning scaled image (Figure 14f).

The process detected the leading shock front for the image sequences from all tests. Ongoing challenges were always detecting an edge at the shock front arrival near the driver troughs of the sinusoidal wave. In this case, our spatial resolution of 4 lp/mm should resolve the troughs. However, the contrast at the troughs associated with 2-mm and 1-mm wavelength drivers was generally insufficient for the gradient magnitude associated with those pixels to exceed the threshold value that properly binarized the other portions of the shock front edge. This issue was not observed for the larger patterns of the 4-mm wavelength drivers. Another challenge occurred when an edge was detected at multiple locations within a single pixel row in the recorded image. An example can be seen in the middle peak of Figure 14d,e as annotated with a red arrow. These cases were treated by only considering the rightmost edge and any subsequent folding of the pattern onto itself was removed along that pixel row.

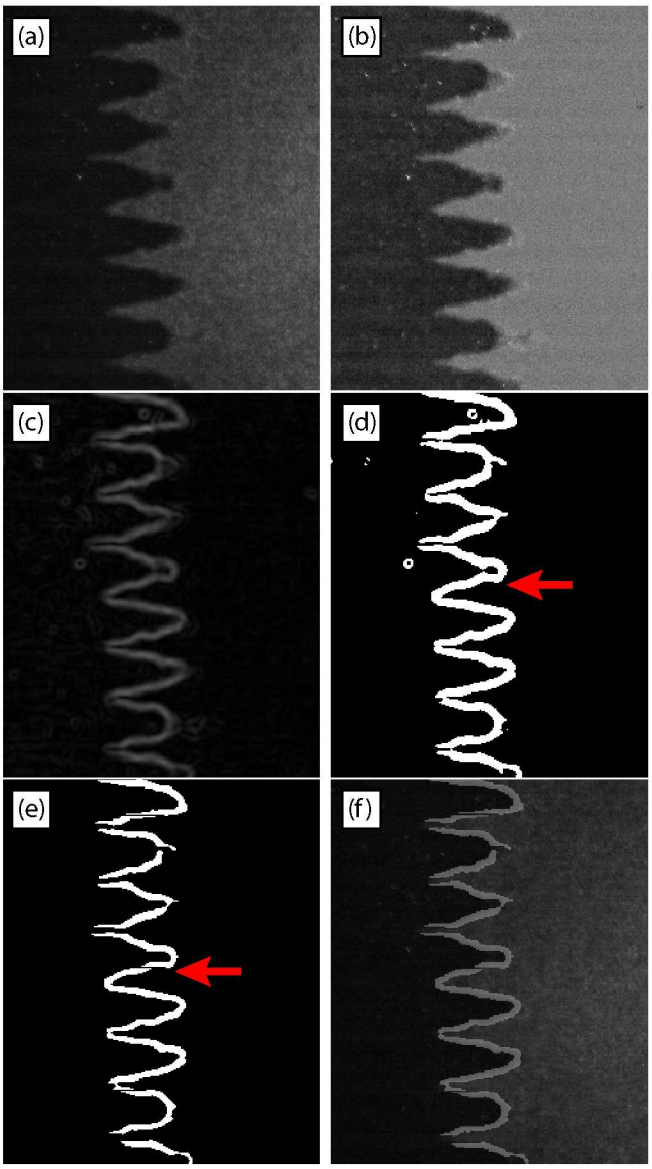

Figure 14. Images describing the post-processing analysis to detect the shock front edge. Images from driver B-3. (a) Raw image, (b) flat field corrected image, (c) gradient magnitude image, (d) binarized image, (e) binarized image after removal of edges not associated with perturbed shock front, and (f) found shock front edge overlaid on raw image. Red arrow denotes a pixel row with two detected edges and only the rightmost edge is retained in the final detected shock front edge.

Once the shock front edge is located, the pixels at each peak and trough of the pattern are determined (Figure 15). To begin, the leading and trailing pixels of the found binary edge (grey points of Figure 15) are fitted with a nearest-neighbor interpolant fit (black line of Figure 15). The pattern middle is determined to facilitate automatic identification of the peak and trough values of the interpolant fit by the *findpeaks()* function of the Signal Processing Toolbox. The result is an array of pixel coordinates (z', y') associated with each peak and trough location on the image (open circles of Figure 15). Using the pixel at the center of the target image and the image magnification, these pixel coordinates are related to spatial position along the window.

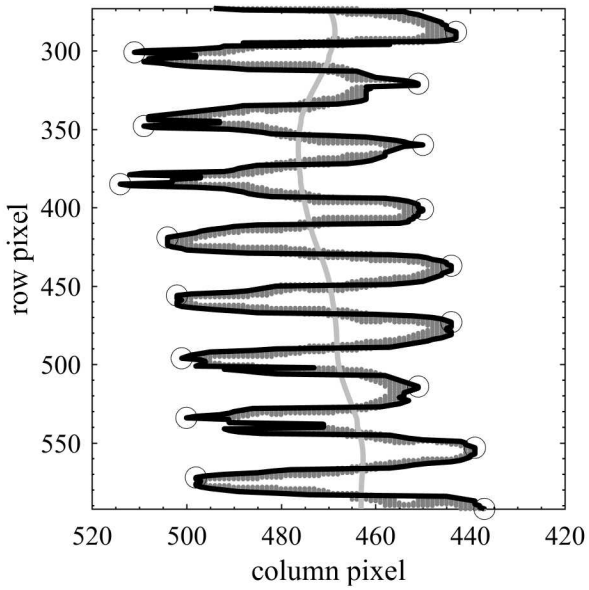

Figure 15. Found edge and peak-to-trough pixel detection in terms of image column pixel (z') and image row pixel (y'). Pixels at the found edge are shown as grey dots. The interpolant fit is shown as a black line that is used to identify the peak and trough locations (open circles). The vertical light gray line is the middle of the found edge.

Spatial position on the window (z', y') is associated with a powder sample thickness $x(z', y')$ based on the target geometry and the pixel at the center of the window (z_0', y_0'). The geometric relationship between sample thickness and position on the window is illustrated in Figure 16. Thus, the additional sample thickness (Δx) processed by the shock propagating in the x-direction appears as a sweeping of the wave across the window $(\Delta z')$. This is calculated with a constant, k, related to the geometry of the target. Finally, the time scale of the perturbed shock (Δt) is calculated from the spatial displacement of the shock front edge on the inclined window and the measured shock velocity (U_s).

$$\Delta t = U_s \Delta x = U_s k \Delta z' \sin\theta \qquad (1)$$

In Figure 16, the wavy pattern modulates along the y-axis direction resulting in many values of $\Delta z'$ for the additional peak-to-trough pairs. To establish a single value for the time scale of the perturbed shock at each frame in the captured image sequence, the average value $(\overline{\Delta z'})$ is used in Eqn. (1). The sample thickness (x) corresponding to this perturbed shock time scale is taken at the center of the visible shock front edge.

$$x = (z_0' - \overline{\Delta z'}) k \sin\theta \qquad (2)$$

These distance-time parameters were nondimensionalized with details of the initial perturbed wave as described in later sections.

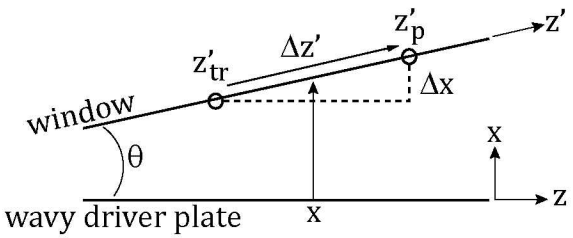

Figure 16. Illustration of geometric relationship between spatial position on window to powder sample thickness for the found edge at one time. The found pixels at the wavy driver peaks (z'_p) and troughs (z'_{tr}) are annotated. The wavy pattern modulates along the y-axis direction.

SHOCK SPEED AND HUGONIOT STATE

The shock speed is calculated from the equivalent sample thickness for the observed distance traveled by the shock front at the inclined window and the interframe time. As the shock moved across the window, these discrete values of shock speed are determined between each peak-to-peak and trough-to-trough pair for all subsequent images of the test. Pairs of data were extracted from the center portion of the round target providing the largest complete dataset extending from toe to heel of the observation surface. This resulted in nominally $n \sim 150$ measurements for each test. The shock speed data were found to be nominally constant with sample thickness and could be fitted with a normal distribution (Figure 17). The shock speed values reported in Table 3 present the mean and standard deviation of the fitted normal distribution. As seen in any of the prior images, significant variation in the edge front is observed. This scatter results in a 12-17% uncertainty on the reported shock speed. The shock speeds are related to the sweep speed or the apparent speed of shock motion across the window ($U_{z'}$) by $U_s = U_{z'} k \sin\theta$. For the measured shock speeds of these experiments, the observed shock motion at the window is on the order of 15 km/s which is significantly greater than the wave speed in the window or any other materials of the target confiner.

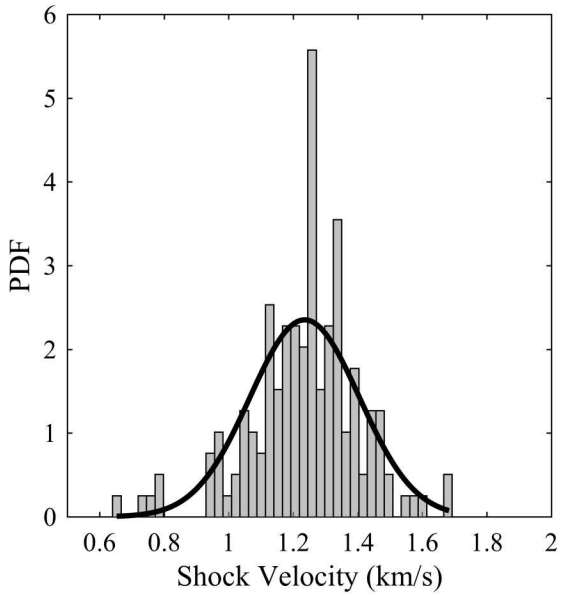

Figure 17. Distribution of shock speeds during shock motion across target for B-3. 150 samples were fitted with a normal distribution to determine the mean value of 1.24 km/s and standard deviation of 0.16 km/s.

Table 3. Calculated shock speeds for tests with 0.9 km/s impact velocity.

WC	1.24 ± 0.16 km/s
Ta	0.97 ± 0.12 km/s
WC/Ta	1.07 ± 0.18 km/s
Cu	1.39 ± 0.10 km/s

The Hugoniot state for the powder samples was determined using the measured shock speeds and impedance matching with the impactor and wavy driver plate. Following the analysis method previously used to analyze WC powders under dynamic planar impact [1], the WC data from these perturbation decay experiments agrees well with the previously reported Hugoniot. The available data from prior studies [1, 12] with new data presented here are shown in Figure 18 as a function of density ρ_H and stress σ_H. The solid black line in Figure 18 is a second order polynomial fit to the WC data [1]. This fit is extrapolated to the ρ_H values of this work and plotted with a dashed line. Refer to the Appendices for the tabulated data.

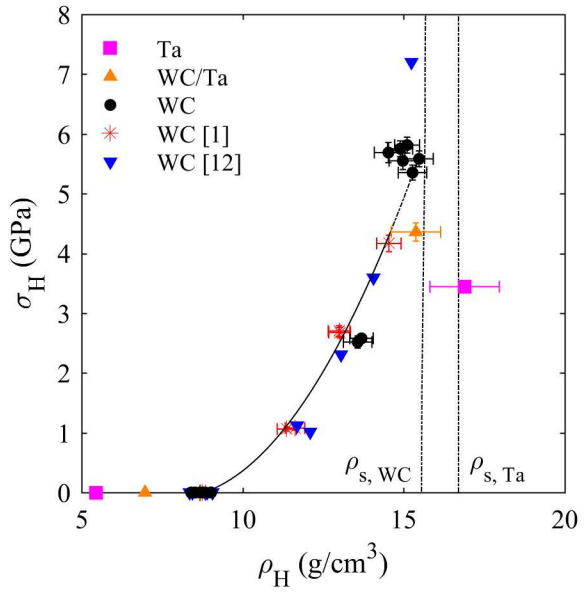

Figure 18. Shock Hugoniot data for WC tests compared to literature [1] and unpublished [12] data. The solid line is a polynomial fit to WC data [1] with dashed line showing extrapolated fit to measured ρ_H of this work. The two tests with Ta and the WC/Ta mixture are also plotted. Data tabulated in Appendices.

The plotted uncertainties are comprised of errors from the initial powder density, impact velocity, the impedance matching method, and shock speeds. Uncertainty in the initial powder density is estimated to be 2%. The uncertainty in the impact velocity is based on the 68% confidence interval of a linear fit to the distance-time data from the target timing pins; nominally less than 1% uncertainty. The uncertainty in the impact velocity is used to determine the uncertainty in the Hugoniot state by impedance matching and is combined with an estimated uncertainty of 2% for the aluminum Hugoniot in this stress regime [1]. The calculated uncertainties in the Hugoniot particle velocity and Hugoniot stress equaled between 2-4%. The Hugoniot density is then calculated from the initial density, Hugoniot particle velocity and shock speed. The uncertainty in shock speed significantly affects the uncertainty in Hugoniot density. The spread in the calculated shock speeds is significant (Table 3), and an error propagation using the standard deviation (σ) assuming a normal distribution results in uncertainties in the Hugoniot density of approximately 10% and for some tests as much as 25-40%. We utilize the knowledge that many samples are fitted by the normal distribution and the uncertainty in the calculated mean is of greatest use in the Hugoniot state calculation. Thus, the propagation of errors calculation uses the standard error of the mean, $\sigma_{\bar{x}} = \sigma/\sqrt{n}$, based on the fitted normal distribution of shock velocity data. This results in uncertainties in the Hugoniot density between 4-10% and the error bars shown in Figure 18. We note that the uncertainties on the individual experiments at approximately 2.8 GPa and 6 GPa are consistent with the scatter across the dataset.

PERTURBATION DECAY

The quantitative data extracted from the image sequences is plotted in nondimensional terms. The perturbation time scale is normalized with $2a_0/U_s - 2a_0/U_{s,d}$. This normalization time corresponds to the maximum perturbation time associated with the shock wave entering the powder sample at the trough and propagating at the measured shock speed (U_s) for a distance equal to the pattern amplitude. This maximum time is reduced by the time for the shock to propagate faster through the driver plate at the shock speed in the aluminum driver ($U_{s,d}$) and enter the powder sample at the pattern peak. The spatial dimension of sample thickness is nondimensionalized with either the perturbation wavelength or the perturbation wavelength and amplitude as discussed in the next sections.

Spatial scaling with perturbation wavelength, x/λ

The perturbation data for WC appears in Figure 19 and contains test data with different impact velocities, pattern wavelength, and pattern amplitude demonstrating a positive correlation of each with perturbation time scale. As the images showed previously (Figure 11), significant variability in the individual peak-to-trough time scale occurs across the field of view in each frame of the captured image sequence. A single value of nondimensionalized Δt (Eqn. 1) and x (Eqn. 2) is plotted for each frame of the test image sequence. The standard deviation associated with the mean peak-to-trough values in each image frame is shown by representative y-axis error bars. The x-axis error bars are plotted but are generally smaller than the symbol size. The mean data show some scatter about a general trend of perturbation decay with increasing sample thickness. This scatter was more significant in the 4-mm datasets. For the three datasets at an impact velocity of 0.9 km/s and 2 mm wavelength, one dataset (E-1) has noticeably smaller values than the other two (B-3, B-4). As shown in Table 2, the E-1 driver plate has a sinusoid amplitude 0.11 mm larger than the driver plates of B-3 and B-4 resulting in the offset datasets when plotted in the scaled terms of Figure 19.

The data also exhibits increased scatter as it just becomes visible at the wedge toe and as it reaches the thickest part of the heel that has not yet been visibly corrupted by the side relief waves. Most datasets show a sharp decrease in perturbation time scale over the last 1 to 4 data points (c.f. WC at 2 mm, 0.5 km/s) – in some cases, this may be preceded by a sharp increase in perturbation time scale. It seems that some artifacts from the three-dimensionality of the powder sample are affecting the data near the toe and heel of the wedge despite no visible detection of relief waves at the observation surface. The perturbed wave would be sensitive to any non-idealities affecting the lateral components of stress in the powder sample.

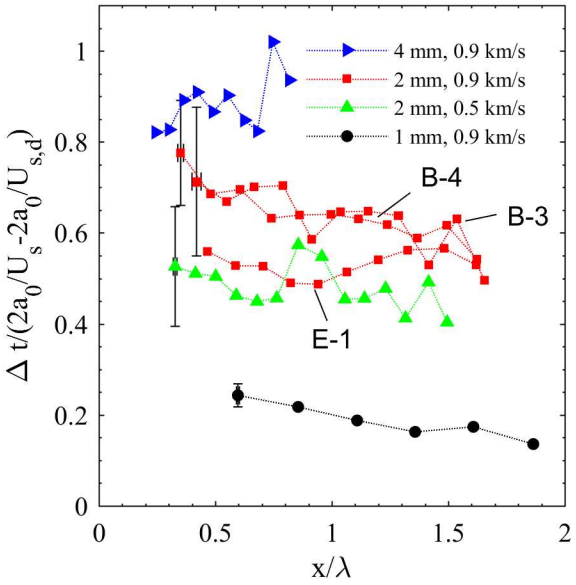

Figure 19. WC data in terms of x/λ scaling and $h = 0.4$ μm. Plotted data for $\lambda = 2$ mm and $U_I = 0.5$ km/s (B-7); $\lambda = 2$ mm and $U_I = 0.9$ km/s (B-3, B-4); $\lambda = 1$ mm and $U_I = 0.9$ km/s (D-1); and multiple-λ driver and $U_I = 0.9$ km/s (E-1).

As mentioned previously, tests were conducted using two different plating thicknesses at the window. Comparison of plating thickness for two WC tests appear in Figure 20. At an impact velocity of 0.5 km/s, no significant difference in perturbation time scale was observed with plating thickness. Qualitatively, the patterns on tests with the thicker plating appeared smoother and had a smaller contrast in pixel intensities across the detected shock edge. These observations suggest some interaction between the particles-plating-window is occurring.

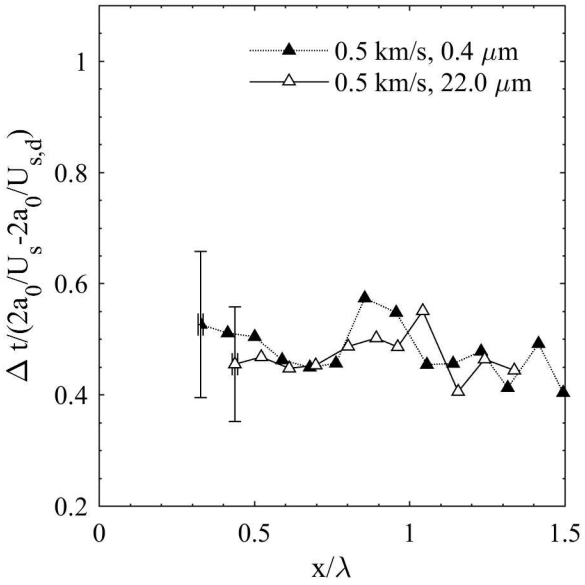

Figure 20. WC data illustrating effect of plating thickness plotted in terms of x/λ scaling and λ = 2 mm. Plotted data for U_I = 0.5 km/s and h= 0.4 μm (B-7), U_I = 0.5 km/s and h= 22 μm (B-11).

One test with a WC/Ta mixture is plotted with the neat WC and Ta data at an equivalent impact velocity and wavelength in Figure 21. The mixture exhibits a greater perturbation decay with increasing sample thickness. This is likely due to the decreased strength of the mixture rather than a density effect.

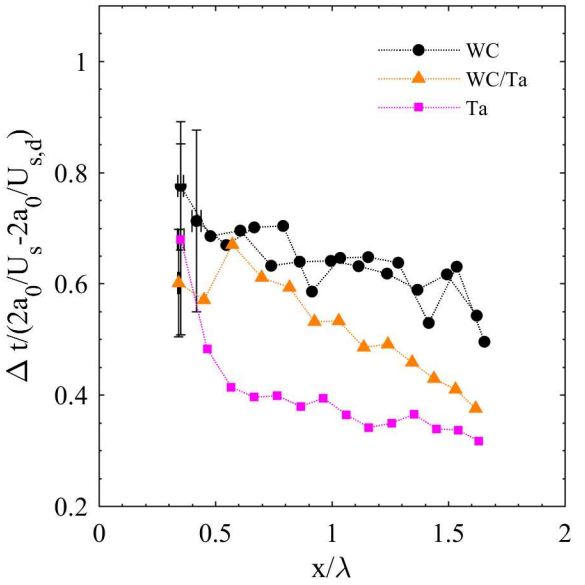

Figure 21. WC and Ta mixture data in terms of x/λ scaling, U_I = 0.9 km/s, h = 0.4 μm, and λ = 2 mm. WC (B-3, B-4), WC/Ta (B-13), and Ta (B-14).

All the neat materials are plotted together in Figure 22. In this plot, the one test conducted with Cu is shown. The perturbed shock in Cu decayed after propagating only half of the observation surface resulting in only four data points. In general, the x/λ scaling does not effectively highlight trends in the powder behavior. A modified scaling for sample thickness is presented in the next section.

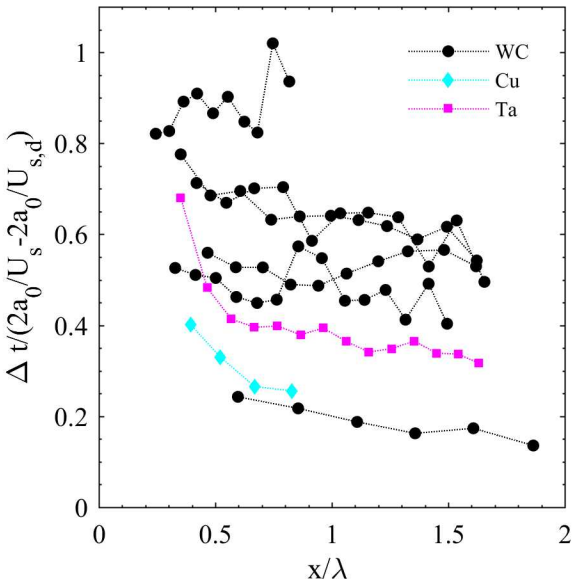

Figure 22. Comparison of all materials in terms of x/λ scaling.

Spatial scaling with perturbation wavelength and amplitude, $x/\lambda(2a_0/\lambda)^2$

Rescaling the perturbation length scale with $x/\lambda\,(2a_0/\lambda)^2$ results in the WC data appearing to follow a single relationship despite the experimental parameters of impact velocity, and pattern wavelength and amplitude. This is demonstrated by comparing Figure 19 with the rescaled data plotted in Figure 23. The data could be fitted with the following functional form,

$$y = (ax + b)/(x^2 + x + b), \qquad (3)$$

with fitted parameters $a = 0.135$ and $b = 0.051$ for the WC data. This functional form was selected as it ensures the scaled perturbation time equals one as sample thickness approaches zero. At large sample thicknesses the perturbation time scale should smoothly and continuously approach zero.

The data of Figure 22 is shown in the log-log plot of Figure 24 along with the calculated fit to the WC data. The scaled data approach one at small values of sample thickness. The data exhibits a slope change for scaled sample thicknesses of 10^{-2} where the scaled perturbation time scale continues to decay with increasing sample thickness. For a comparison between the powders, the Cu and Ta exhibit a lower perturbation time scale at an equivalent sample thickness. More tests are needed to understand if the rate of perturbation decay with increasing

thickness remains consistent between materials. The relationship of the data between the different materials does not appear ordered with initial density or particle size (Table 1). Future work is needed to identify the critical parameter of the powder that dominates the perturbation behavior.

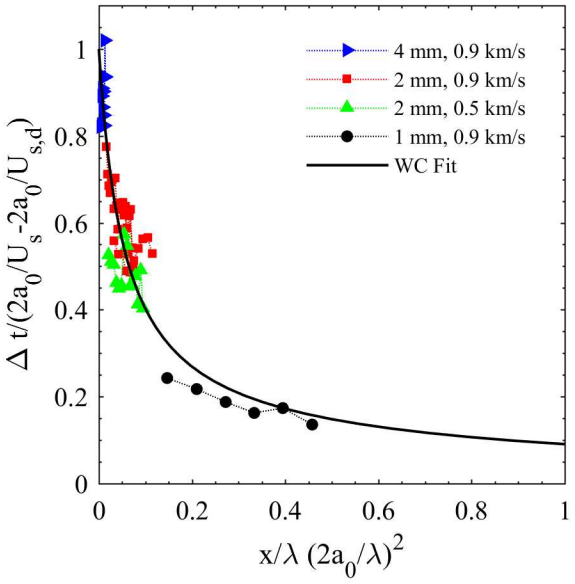

Figure 23. WC data with alternate scaling. WC fit from Eqn. (3).

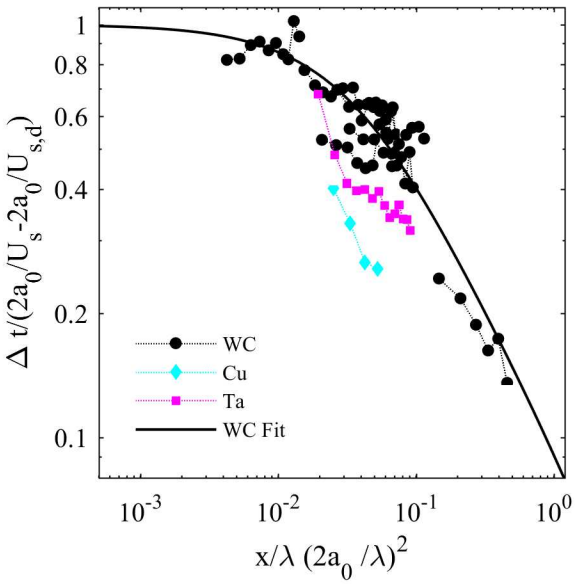

Figure 24. All materials plotted on a log-log plot with alternate scaling for sample thickness. Fitted relationship, Eqn. (3), for WC material also plotted.

Continuum and mesoscale simulations of the experiment were performed previously [5] and are plotted with the WC data in Figure 25. The mesoscale simulations assumed spherical particles with uniform diameter equal to 32 μm of WC, a simple Mie-Grüneisen equation of state and an elastic perfectly plastic strength model. The

continuum model treated the compaction of the powder sample with a P-λ model and treated the strength of the powder sample with a pressure-dependent yield strength model (referred to as the Geo strength model, GSM). In the GSM model, the yield strength with pressure is varied by changing model parameter dY/dP. The mesoscale simulations show the best comparison to the experimental data for x-axis values greater than 5×10^{-2}. The continuum model results display representative trends and it appears that a higher model strength value (dY/dP) would represent the experimental data well for larger sample thicknesses. For both the mesoscale and continuum models, extending the simulations to x-axis values approaching 10^{-3} is needed to explore how the simulated results behave in the limit as sample thickness goes to zero.

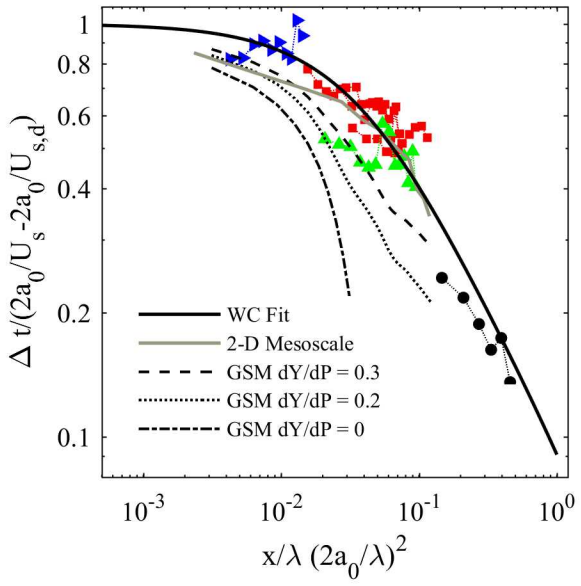

Figure 25. Comparison of WC data with continuum and mesoscale simulations [5].

CONCLUSION

Data of perturbed shock damping behavior in powders was collected within shock regimes by projectile impact with wavy plate and a cylindrical wedge of powder at its tap density. Novel to this experiment was high speed imaging of the wavy pattern of the transmitted shock wave at the inclined wedge surface. By pulsing the laser illumination, the short effective image exposures captured an abrupt contrast change at the shock front for quantitative post-processing. These images also provided new observations of additional spatial disturbances on the perturbed shock front dependent on particle shape and morphology. Shock arrival and its perturbed front shape were imaged for various metal powders varying parameters of perturbation amplitude and wavelength. Post-test image processing extracted quantitative data of the material Hugoniot state, and decay in the perturbation time scale with shock propagation through increasing powder thickness. For a given material and appropriate nondimensionalization, multiple experiments varying impact velocity and initial perturbation features are plotted

together with a single functional relationship. Good agreement between the experimental data and continuum simulations showed that an appropriately chosen value for the pressure-dependent yield strength is a reasonable approximation. Efforts in expanding the continuum simulation results are the subject of future work, in addition to collecting experimental data with different mixture ratios to further explore the effects of bulk density and particle strength.

ACKNOWLEDGEMENTS

The authors gratefully acknowledge the experimental contributions and mentorship of Wayne Trott. Heidi Anderson is gratefully acknowledged for construction of the target assemblies. This paper describes objective technical results and analysis. Any subjective views or opinions that might be expressed in the paper do not necessarily represent the views of the U.S. Department of Energy or the United States Government. Sandia National Laboratories is a multimission laboratory managed and operated by National Technology and Engineering Solutions of Sandia, LLC, a wholly owned subsidiary of Honeywell International, Inc., for the U.S. Department of Energy's National Nuclear Security Administration under contract DE-NA-0003525.

APPENDIX A. TEST MATRIX FOR WC TESTS

Test Number	692	693	696	698	705	706	707	709	715
Driver Plate	B-3	B-4	B-7	B-9	C-1	D-1	B-11	F-1	E-1
Image Scale (px/mm)	20.432	19.629	20.533	20.533	20.087	20.087	20.087	NA	21.488
Impact Velocity (km/s)	0.879 ± 0.002	0.890 ± 0.001	0.509 ± 0.005	0.888 ± 0.001	0.889 ± 0.001	0.889 ± 0.001	0.512 ± 0.001	0.893 ± 0.003	0.885 ± 0.004
Powder Density (g)	8.74	8.84	8.52	8.40	8.80	9.02	8.67	8.69	8.69
Pattern Amplitude, $2a_0$(mm)	0.416	0.417	0.499	0.507	0.516	0.490	0.456	0	0.526
Pattern Wavelength, λ (mm)	1.982[a]	1.982[a]	1.982[a]	1.983	3.962	0.989	1.981	Inf	1.979 3.988
Plating Thickness (μm)	0.4	0.4	0.4	21.9	21.9	0.4	22.8	0.4	0.4
Shock Speed in Powder Sample, U_s(km/s)	1.24	1.27	0.89	1.19	1.21	1.27	0.90	NA	1.28
Shock Speed in Powder Sample Standard Deviation, σ(km/s)	0.17	0.15	0.20	0.15	0.13	0.07	0.17	NA	0.20
Shock Speed in Powder Sample Standard Error of Mean, $\sigma_{\bar{x}}$(km/s)	0.01	0.01	0.01	0.01	0.01	0.01	0.02	NA	0.02
Shock Speed in Driver Plate, $U_{s,d}$(km/s)	5.98	5.98	5.77	5.98	5.98	5.98	5.77	5.98	5.98
Hugoniot state, u_H(km/s)	0.51 ± 0.01	0.51 ± 0.01	0.33 ± 0.01	0.54 ± 0.01	0.52 ± 0.01	0.51 ± 0.01	0.33 ± 0.01	NA	0.51 ± 0.02
Hugoniot state, σ_H(km/s)	5.55 ± 0.15	5.75 ± 0.13	2.52 ± 0.10	5.35 ± 0.12	5.58 ± 0.13	5.81 ± 0.13	2.58 ± 0.06	NA	5.69 ± 0.17
Hugoniot state, ρ_H(km/s)	14.97 ± 0.43	14.89 ± 0.39	13.57 ± 0.44	15.27 ± 0.44	15.48 ± 0.44	15.10 ± 0.39	13.69 ± 0.36	NA	14.52 ± 0.44

[a] Based on manufacturing drawing nominal tolerance; not profilometer measured quantity

APPENDIX B. TEST MATRIX FOR CU, TA, WC/TA TESTS

Test Number	695	718	714
Driver Plate	B-6	B-14	B-13
Material	Cu	Ta	WC/Ta
Image Scale (px/mm)	18.480	18.480	20.087
Impact Velocity (km/s)	0.893 ± 0.006	0.891 ± 0.003	0.878 ± 0.006
Powder Density (g)	5.50	5.45	6.97
Pattern Amplitude, $2a_0$(mm)	0.501	0.462	0.465
Pattern Wavelength, λ (mm)	1.982[a]	1.961	1.975
Plating Thickness (μm)	0.4	0.4	0.4
Shock Speed in Powder Sample, U_s(km/s)	1.39	0.97	1.07
Shock Speed in Powder Sample Standard Deviation, σ(km/s)	0.10	0.12	0.18
Shock Speed in Powder Sample Standard Error of Mean, $\sigma_{\bar{x}}$(km/s)	0.02	0.01	0.02
Shock Speed in Driver Plate, $U_{s,d}$(km/s)	5.99	5.98	5.98
Hugoniot state, u_H(km/s)	0.59 ± 0.02	0.65 ± 0.02	0.59 ± 0.02
Hugoniot state, σ_H(km/s)	4.52 ± 0.16	3.44 ± 0.09	4.36 ± 0.15
Hugoniot state, ρ_H(km/s)	9.58 ± 0.33	16.88 ± 1.08	15.38 ± 0.77

[a] Based on manufacturing drawing nominal tolerance; not profilometer measured quantity

REFERENCES

[1] T. J. Vogler, M. Y. Lee and D. E. Grady, "Static and dynamic compaction of ceramic powders," *International Journal of Solids and Structures,* vol. 44, pp. 636-658, 2007.

[2] M. A. Cooper, A. L. Brundage and E. C. Dudley, "Static and Dynamic Compaction of CL-20 Powders," *AIP Conference Proceedings,* vol. 1195, p. 1385, 2009.

[3] M. G. Briscoe and A. A. Kovitz, "Experimental and theoretical study of the stability of plane shock waves reflected normally from perturbed flat walls," *Journal of Fluid Mechanics,* vol. 31, no. 3, pp. 529-546, 1968.

[4] V. N. Mineev and E. V. Savinov, "Viscosity and Melting Point of Aluminum, Lead, and Sodium Chloride Subjected to Shock Compression," *Soviet Physics JETP,* vol. 25, no. 3, pp. 411-416, 1968.

[5] T. J. Vogler, "Shock wave perturbation decay in granular materials," *Journal of Dynamic Behavior,* vol. 1, no. 4, pp. 370-387, 2015.

[6] X.-J. Ma, F.-S. Liu, M.-J. Zhang and Y.-Y. Sun, "Viscosity of aluminum under shock-loading conditions," *Chinese Physics B,* vol. 20, no. 6, p. 068301, 2011.

[7] M. Gresshoff, M. Oldaker, D. M. Hoffman, K. J. McMullen, G. E. Overturf III, P. Pagoria and M. X. Zhang, "A New Light Enhancement Coating Formulation to be used for TATB Detonation Front Detection," *Proceedings of the 15th International Detonation Symposium,* no. LLNL-PROC-656558, 2014.

[8] D. D. Bloomquist and S. A. Sheffield, "Optically recording interferometer for velocity measurements with subnanosecond resolution," *Journal of Applied Physics,* vol. 54, no. 4, pp. 1717-1722, 1983.

[9] M. A. Cooper, "Optically recording velocity interferometer system configurations and impact of target surface reflectance properties," *Applied Optics,* vol. 53, no. 24, pp. F21-F30, 2014.

[10] S. Opie, E. Loomis, P. Peralta, T. Shimada and R. P. Johnson , "Strength and Viscosity Effects on Perturbed Shock Front Stability in Metals," *Physical Review Letters,* vol. 118, no. 19, p. 195501(5), 2017.

[11] J. P. Borg and T. J. Vogler, "Mesoscale calculations of the dynamic behavior of a granular ceramic," *International Journal of Solids and Structures,* vol. 45, no. 6, pp. 1676-1696, 2008.

[12] T. J. Vogler, *personal communication.*

[13] W. M. Trott, M. R. Baer, J. N. Castaneda, L. C. Chhabildas and J. R. Asay, "Investigation of the mesoscopic scale response of low-density pressings of granular sugar under impact," *Journal of Applied Physics,* vol. 101, p. 024917, 2007.